JOURNAL OF PROPULSION AND POWER
Vol. 25, No. 2, March–April 2009

New Simulation Strategy for an Oscillating Cascade in Turbomachinery Using Immersed-Boundary Method

Guohua Zhong* and Xiaofeng Sun†
Beijing University of Aeronautics and Astronautics, 100083 Beijing, People's Republic of China

DOI: 10.2514/1.35347

Based on the immersed-boundary method, a numerical simulation for an oscillating cascade is established and the relevant analysis is presented with emphasis on the physical understanding of fluid–structure interaction. To validate the method, two simulation cases, an oscillating circular cylinder at a low Keulegan–Carpenter number and a flapping airfoil, are performed and the results are in good agreement with the previous research. In the oscillating cascade simulation, it is found that the reduced velocity U^* is a very sensitive factor which affects the critical stable boundary in the present examples. On the other hand, the effects of interblade phase angles on the system stability are also discussed. In particular, it is worth noting that the same process is applied to several test cases without generating any body-fitting grid. Therefore, the method shows a significant time savings in the computational process for such a complicated fluid–structure interaction problem.

Nomenclature

A	=	cylinder oscillation amplitude
A_0	=	translational amplitude
C_{damping}	=	damping coefficient
C_D	=	drag coefficient
C_L	=	lift coefficient
C_M	=	rotational moment coefficient
c_h	=	structural damping ratio in transverse direction
c_θ	=	structural damping ratio in rotational direction
D	=	diameter of the cylinder
$F(\mathbf{x}, t)$	=	external force
F_h	=	lift in transverse direction
F_θ	=	moment around the airfoil elastic center
f	=	oscillating frequency
$f(\mathbf{x}_s, t)$	=	force per unit area applied by the body to the fluid
f_n	=	natural frequency of the oscillating blade
h	=	transverse movement displacement
$\dot{h}$	=	transverse movement velocity
$\ddot{h}$	=	transverse movement acceleration
h_x	=	mesh size in x direction
h_y	=	mesh size in y direction
I_θ	=	inertial moment around the airfoil elastic center
KC	=	Keulegan–Carpenter number
k_h	=	structural stiffness ratio in transverse direction
k_θ	=	structural stiffness ratio in rotational direction
l	=	reference length
m	=	mass of the airfoil
m^*	=	nondimensional mass of the body
$p(\mathbf{x}, t)$	=	flow pressure
Re	=	Reynolds number
r	=	length between surface point and elastic center
S_θ	=	static moment around the airfoil elastic center
T	=	overall period of the system
$U(\mathbf{x}, t)$	=	flow velocity
$U(\mathbf{x}_s, t)$	=	flow velocity on the body surface
$U_{\max}$	=	maximum velocity of the cylinder motion
U_∞	=	uniform flow velocity
U^*	=	reduced velocity
$v(\mathbf{x}_s, t)$	=	body surface velocity
$\mathbf{x}$	=	computational mesh coordinates
$\mathbf{x}_s$	=	body surface coordinates
x	=	Cartesian components of $\mathbf{x}$
$x(t)$	=	translation motion position
$x'(t)$	=	translation motion velocity
y	=	Cartesian components of $\mathbf{x}$
α	=	feedback function negative constants
α_0	=	rotational initial angle
β	=	feedback function negative constants
β_0	=	rotational amplitude
Γ	=	airfoil surface
δ	=	two-dimensional delta function
ζ	=	structural damping ratio
θ	=	rotational angle
$\dot{\theta}$	=	rotational angular velocity
$\ddot{\theta}$	=	rotational angular acceleration
ρ_∞	=	density of fluid
Φ	=	difference phase between $x(t)$ and $\alpha(t)$
$\phi(r)$	=	function to construct δ

Received 28 October 2007; accepted for publication 17 October 2008.

*Ph.D. Candidate, School of Jet Propulsion, No. 37, Xueyuan Road; zgh@buaa.edu.cn.

†Professor, School of Jet Propulsion, No. 37, Xueyuan Road; Sunxf@buaa.edu.cn.

I. Introduction

THE compressor/turbine blade rows flutter has become one of the critical problems with the development of the modern aircraft engine. The oscillating cascade, generally as a typical nonlinear fluid–structure interaction, is attracting increasing attention in both aeroelasticity and unsteady aerodynamic fields.

This kind of unsteady phenomenon is usually described with the terms "fluid induced oscillation" and "self-excited oscillation," which involve the interaction between an unsteady fluid flow and an oscillating cascade. To improve the physical understanding of fluid–structure interaction for various practical applications, it is noted that many relevant engineering designs need a more accurate and reliable fluid–structure interaction model. Obviously it is necessary to develop an efficient, robust, and fully coupled numerical simulation method for the fluid–structure interaction such as an oscillating airfoil problem. On the other hand, the rapid development of active/passive control techniques [1–6] for cascade flutter requires more detailed description of the flowfield and structure response to build up a more accurate and high efficient stability model. However, we see that it is not easy to fully meet these requirements in both past and current investigations [7–10].

In fact, the aerodynamic behavior and the structural behavior were treated in a decoupled way in the early stages, that is, solve the

unsteady flowfield around the oscillating airfoil and apply the energy method to determine if the aerodynamic forces damp or amplify the oscillation, supposing the airfoil oscillating frequency is fixed and the motion is given. These methods provide some physical explanation as well as a reasonable prediction of the stability behavior of the system but seem to be incapable of simulating a complex aeroelastic coupling phenomena. Besides, the modern treatment [11–18] of oscillating cascade simulation divides the computation into two parts, which are fluid flow simulation and structure deformation simulation. In fluid domain, we usually generate a body-fitting grid and solve the unsteady Navier–Stokes equations. In structure domain, the structure deformation and the solid displacement are calculated and then the fluid domain provides the aerodynamic force information to the structure domain, which transmits the boundary position and solid body velocity to the fluid domain. The time cost for grid generation and information communication is negligible if the airfoil stays stationary during the time span of simulation, but for time-varying flutter simulation that requires regriding to accommodate changes in the airfoil deformation or displacement, this approach will incur significant penalties. A grid-stretching technique is a choice for relatively simple motions, but appears still slow and the grid quality near the moving airfoil is hard to control.

The above analysis, on one hand, shows great progress in handling this problem. On the other hand, it also reveals that how to realize the real fluid–structure coupling simulation and how to avoid regridding for a moving boundary are still challenging problems. Therefore, any new attempt toward overcoming these difficulties may be required. Flow and the oscillating airfoil impose boundary conditions on each other, so the idea of taking the fluid and structural dynamics as a single system may result in more convenient and time-saving methods. The immersed-boundary method, first developed by Peskin [19,20] avoids regridding for a moving boundary and thus becomes a promising scheme for complex and moving geometries. This method has been widely expanded and implemented in various research fields [21–25]. Fadlun et al. [22] developed a second-order accuracy scheme to simulate a full three-dimensional complex flow inside an internal combustion piston/cylinder assembly at a high Reynolds number. Zhu and Peskin [23] simulated flow past two flexible, flapping filaments in a flowing soap film. Miller and Peskin [24] modeled a two-dimensional tiny insect wing through a one stroke cycle to study changes in lift generation and vortex dynamics. Kalitzin and Iaccarino [25] developed a ghost-cell-based immersed-boundary method to simulate the flow past a pickup truck. Mittal et al. [26] employed a cut-cell-based immersed-boundary method to examine the dynamics of plates falling freely in a fluid under the influence of gravity. However, to the authors' knowledge, there is no work related to the oscillating cascade simulation. We realize that this method may be a good choice for such a fluid–structure interaction problem. Especially, more emphasis will be placed on a better physical understanding of the fluid–structure coupling mechanism.

We develop a numerical solver aiming at the computation of an oscillating cascade. It is obvious that the code must be carefully validated before the simulation of an oscillating cascade problem. In this paper, we choose two kinds of fluid–structure interaction phenomena such as the benchmark problems. An oscillating circular cylinder in fluid at rest has been a subject of research. The physical essence is the fluid motion induced by the oscillation of the cylinder. It is a typical fluid-structure interaction problem, in which it is difficult to use traditional methods due to its geometric complexity and movement inside the flow. In this case, the oscillating cylinder induces turbulence in the flow and turbulence induces vibration on the cylinder. Another case selected to validate the method is the flapping airfoil [27,28], which is similar to a flapping elliptical airfoil in fluid at rest. We obtained good agreement with previous research in the two benchmark cases; two sets of computations for the oscillating cascade are then established and the relevant analysis to the behavior of the cascade at different reduced velocity and different interblade phase angles (IBPA) are presented with emphasis on the physical understanding of the fluid-cascade interaction.

II. Fluid Dynamic Model and Its Solution

We write the two-dimensional, incompressible Navier–Stokes equations with an external force field as

$$\frac{\partial \mathbf{u}(\mathbf{x},t)}{\partial t} + (\mathbf{u}(\mathbf{x},t)\cdot\nabla)\,\mathbf{u}(\mathbf{x},t) = -\nabla p(\mathbf{x},t) + \frac{1}{Re}\nabla^2\mathbf{u}(\mathbf{x},t) + \mathbf{F}(\mathbf{x},t) \tag{1}$$

and continuity equation as

$$\nabla\cdot\mathbf{u}(\mathbf{x},t) = 0 \tag{2}$$

where Re is the Reynolds number, and $F(\mathbf{x},t)$ is the external force.

The equation are discretized spatially in the transverse (y) and streamwise (x) directions by second-order central finite differences. Operator splitting techniques are applied to decompose Eq. (1) into four simpler problems temporally and treat them separately using specialized numerical algorithms. We can show the four steps as

$$\mathbf{u}(\mathbf{x},t) \to \mathbf{u}(\mathbf{x},t+\mathrm{d}t/4) \to \mathbf{u}(\mathbf{x},t+\mathrm{d}t/2) \to \mathbf{u}(\mathbf{x},t+3\,\mathrm{d}t/4) \to \mathbf{u}(\mathbf{x},t+\mathrm{d}t) \tag{3}$$

The first step is to solve the convection term $[\mathbf{u}(\mathbf{x},t) \to \mathbf{u}(\mathbf{x},t+\mathrm{d}t/4)]$ by the explicit third-order compact Runge–Kutta method,

$$\frac{\partial \mathbf{u}(\mathbf{x},t+\mathrm{d}t/4)}{\partial t} = -(\mathbf{u}(\mathbf{x},t)\cdot\nabla)\mathbf{u}(\mathbf{x},t) \tag{4}$$

The second step is to solve the external force field term $[\mathbf{u}(\mathbf{x},t+\mathrm{d}t/4) \to \mathbf{u}(\mathbf{x},t+\mathrm{d}t/2)]$ by the direct time integration,

$$\frac{\partial \mathbf{u}(\mathbf{x},t+\mathrm{d}t/2)}{\partial t} = \mathbf{F}(\mathbf{x},t+\mathrm{d}t/4) \tag{5}$$

The third step is to solve the diffusion term $[\mathbf{u}(\mathbf{x},t+\mathrm{d}t/2) \to \mathbf{u}(\mathbf{x},t+3\,\mathrm{d}t/4)]$ by the Peacemen–Rachford scheme,

$$\frac{\partial \mathbf{u}(\mathbf{x},t+3\,\mathrm{d}t/4)}{\partial t} = \frac{1}{Re}\nabla^2\mathbf{u}(\mathbf{x},t+\mathrm{d}t/2) \tag{6}$$

And then, solve the pressure Poisson equation $[\mathbf{u}(\mathbf{x},t+3\,\mathrm{d}t/4) \to \mathbf{u}(\mathbf{x},t+\mathrm{d}t)]$ by the matrix diagonalization method,

$$\nabla^2 p(\mathbf{x},t+\mathrm{d}t) = \frac{1}{\Delta t}\nabla\cdot\mathbf{u}(\mathbf{x},t+3\,\mathrm{d}t/4) - \nabla\cdot\mathbf{F}(\mathbf{x},t+3\,\mathrm{d}t/4) \tag{7}$$

And the last, use $p(\mathbf{x},t+\mathrm{d}t)$ to update the velocity field

$$\mathbf{u}\,(\mathbf{x},t+\mathrm{d}t) = \mathbf{u}(\mathbf{x},t+3\,\mathrm{d}t/4) - \Delta t\cdot\nabla p(\mathbf{x},t+\mathrm{d}t) \tag{8}$$

The external force term $F(\mathbf{x},t)$ requires some explanation. We use the methods introduced by Goldstein et al. [29] and Saiki and Biringen [30]. To introduce the basic principles of the immersed-boundary method, the details are defined by Eqs. (9–13). Assuming that a body is immersed in the fluid, we further require that the velocity field on the boundary should satisfy the nonslip boundary condition for fluid velocity on the body surface, which equals the velocity of the body itself, as defined in Eq. (10). The immersed-boundary methods ensure such boundary condition by introducing an additional body force term into the Navier–Stokes equation, which represents a singular Dirac delta function on the fluid-structure interface. We need to first find the force distribution corresponding to the required boundary condition and then spread the force to the flowfield. Thus the effect of a solid boundary to the fluid is properly simulated by a force field. In the discrete numerical implementation of the idea above, the interface is discretized as a set of points immersed in the flowfield domain, which is also discretized. The description of boundary movement can be simply done by changing

the coordinates of boundary points without any adjustment to the basic grid, so the immersed-boundary methods do not incur a significant additional time cost for regridding. In addition, because there is no restriction to the background grid for the flowfield, a regular Cartesian or cylindrical grid can be chosen to simplify the mesh mapping and acquire relatively high accuracy. The force $F(\mathbf{x}, t)$ is governed by the following functions:

$$\mathbf{U}(\mathbf{x}_s, t) = \int \mathbf{U}(\mathbf{x}, t)\delta(\mathbf{x} - \mathbf{x}_s)\, d\mathbf{x} \tag{9}$$

$$f(\mathbf{x}_s, t) = \alpha \int_0^t [\mathbf{U}(\mathbf{x}_s, t) - v(\mathbf{x}_s, t)]\, dt + \beta[\mathbf{U}(\mathbf{x}_s, t) - v(\mathbf{x}_s, t)] \tag{10}$$

$$F(\mathbf{x}, t) = \int f(\mathbf{x}_s, t)\delta(\mathbf{x} - \mathbf{x}_s)\, d\mathbf{x}_s \tag{11}$$

$$\delta(\mathbf{x}) = \frac{1}{h_x h_y}\phi\left(\frac{x}{h_x}\right)\phi\left(\frac{y}{h_y}\right) \tag{12}$$

$$\begin{aligned}
&\phi(r) = 0 \\
&r \le -2 = \tfrac{1}{8}(5 + 2r - \sqrt{-7 - 12r - 4r^2}), -2 \le r \\
&\quad \le -1 = \tfrac{1}{8}(3 + 2r + \sqrt{1 - 4r - 4r^2}), -1 \le r \\
&\quad \le 0 = \tfrac{1}{8}(3 - 2r + \sqrt{1 + 4r - 4r^2}), 0 \le r \\
&\quad \le 1 = \tfrac{1}{8}(5 - 2r - \sqrt{-7 + 12r - 4r^2}), 1 \le r \le 2 = 0 \\
&2 \le r
\end{aligned} \tag{13}$$

Similar to Peskin [31], $\delta(\mathbf{x})$ is a two-dimensional delta function. In the following simulation cases, α is -4000 and β is -60. The negative constants α and β are determined by the flowfield and the flow solver [29]. As described by Saiki and Biringen [30], α must produce a response with a natural frequency greater than the highest frequencies which present in the flow so that $F(\mathbf{x}, t)$ can respond correctly to the varying flowfield. Different combinations of α and β have been tested in a flow past a stationary cylinder case. Although different combinations of α and β would add different forcing functions to the boundary, the flowfield results are slightly different and the higher values of α and β make the feedback function respond faster to the unsteady flowfield and act efficiently in reinforcing the boundary condition.

III. Computational Results and Analysis

A. Oscillating Circular Cylinder

This section introduces a numerical study of the fluid motion induced by the oscillation of a circular cylinder in a two-dimensional square domain. The translational motion of the cylinder is defined as

$$x(t) = -A\sin(2\pi f t) \tag{14}$$

The Keulegan–Carpenter number KC is defined as

$$KC = \frac{U_{\max}}{fD} \tag{15}$$

The diameter of the cylinder is 1 and the computational domain is a 16×16 square, which is divided into a 300×300 mesh (see Fig. 1). The Reynolds number is set to 100 in this case, with the reference length and velocity chosen to be the diameter and the maximum instant velocity of the cylinder. Nonshear conditions are assumed for all four boundaries of the computational domain: $\frac{\partial u}{\partial y} = 0$, $v = 0$ for lower and upper boundaries and $\frac{\partial v}{\partial x} = 0$, $u = 0$ for left and right boundaries, and the boundary condition for the cylinder interface is the nonslip condition. The cylinder position is supposed at its maximum amplitude (left side) and the cylinder started from rest as the initial condition.

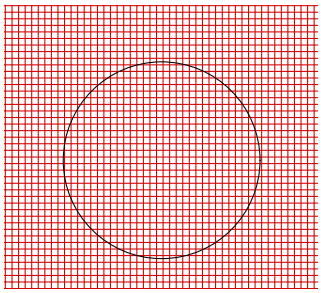

Fig. 1 Computational grid of an oscillating circular cylinder in water at rest.

Figure 2 shows the comparison of drag forces between the current result and the previous experimental data. It should be noted that our simulation included a filter technique to remove high frequency noise. The filter step can be applied to the resulting data similar to the drag and lift coefficients as done by Miller and Peskin [24] or to the parameters during the computation by Xu and Wang [32]. From Fig. 2, good agreement is found between the present numerical results and the data reported by Dutsch et al. [33].

B. Flapping Airfoil

In this case, the fluid motion is induced by a flapping airfoil. For an elliptical airfoil of aspect ratio 10 flapping in the horizontal plane and rotating about its spanwise axis, the translational and rotational motion are defined as

$$x(t) = \tfrac{1}{2}A_0\cos(2\pi f t) \tag{16}$$

$$\theta(t) = \alpha_0 + \beta_0\sin(2\pi f t + \Phi) \tag{17}$$

The maximum translational airfoil velocity of the airfoil centroid, $U_{\max}$, is $\pi f A_0$ and A_0 is set to 2.8. The Reynolds number is set to 75, with the reference length and velocity chosen to be the chord length and $U_{\max}$. Φ is set to $\pi/4$ and 0; the other parameters α_0, β_0, and f are set to $\pi/2$, $\pi/4$, and 0.25. The square computational domain $\Omega = 15 \times 15$ with the mesh point 400×400 is applied. The boundary condition is similar to the oscillating circular cylinder case.

Figure 3 shows the time evolution of drag and lift coefficients with phases 0 and $\pi/4$, respectively, normalized by maximum quasi-steady values [28], compared with the previous results. From the figures, it can be seen that the current results are in good agreement

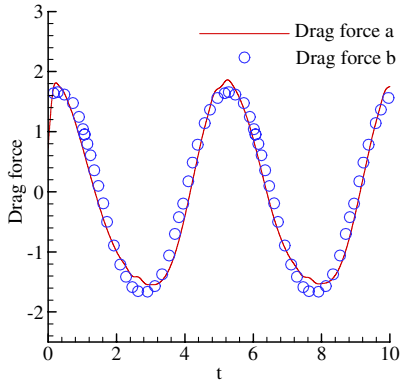

Fig. 2 Drag force comparison of an oscillating circular cylinder in water at rest. a: 500 point FFT smoothing of present work; b: Dutsch et al. [33].

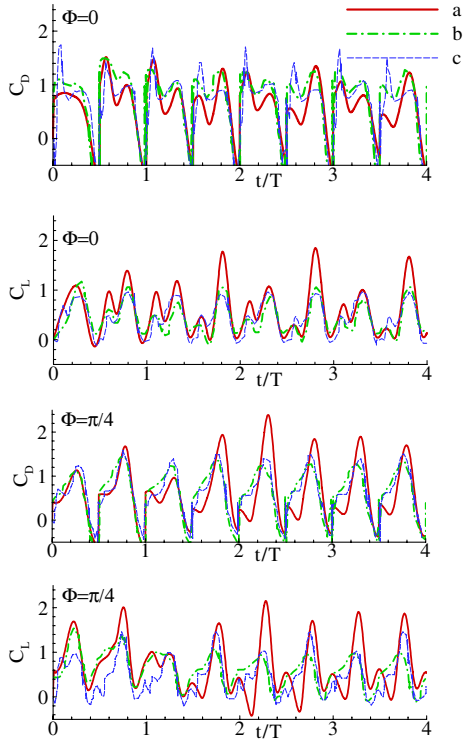

Fig. 3 The time evolution of lift and drag coefficients with phase 0 and phase $\pi/4$. a: Present work; b: numerical work [28]; c: experimental work [28].

with the previous results except for the amplitudes of the drag and lift coefficient peaks. The present resulting averaged lift and drag are 0.869 and 1.308 for phase $\pi/4$, and 0.833 and 1.293 for phase 0, respectively, whereas experimental results reported by Wang et al. [28] are 0.93 and 1.28 for phase $\pi/4$, and 0.86 and 1.34 for phase 0, respectively. This means that our numerical results are in relatively good agreement with the experimental data. The computational lift and drag coefficient results by Wang et al. are (1.10, 1.36) and (0.82, 1.44) for the corresponding cases.

From the comparison and analyses as above, our numerical method and code can provide reasonable computational accuracy for several moving boundary problems. It is important to note that the use of the immersed-boundary method in these problems does reveal obvious advantages, particularly in its simple mesh generation. Ignoring the mesh regeneration in each time step means that computational time cost has been reduced. Based on the checks above, we will extend its application to the oscillating airfoil case in the following section.

C. Oscillating Cascade

As shown in Fig. 4, the oscillating cascade consists of five blades. Each individual blade has 2 degrees of freedom: h and θ. This simulation case is divided into two sets. All the other blades are assumed to follow the motion of a prescribed blade, such as the third blade in synchronal or phase-lagged mode. For the third blade, similar to Piperno [34], the nondimensional equations for evolution of the third blade motion are given as follows:

$$m\ddot{h} + S_\theta \ddot{\theta} + c_h \dot{h} + k_h h = F_h \tag{18}$$

$$S_\theta \ddot{h} + I_\theta \ddot{\theta} + c_\theta \dot{\theta} + k_\theta \theta = F_\theta \tag{19}$$

All parameters in Eqs. (18) and (19) are described as

$$\begin{aligned} &b = c/2, \quad \omega_h = \lambda \omega_\theta, \quad k_h = m\omega_h^2, \quad c_h = 2\xi_h \omega_h m \\ &S_\theta = mbx_\theta, \quad I_\theta = mb^2\gamma_\theta^2, \quad k_\theta = I_\theta \omega_\theta^2, \quad c_\theta = 2\xi_\theta \omega_\theta I_\theta \end{aligned} \tag{20}$$

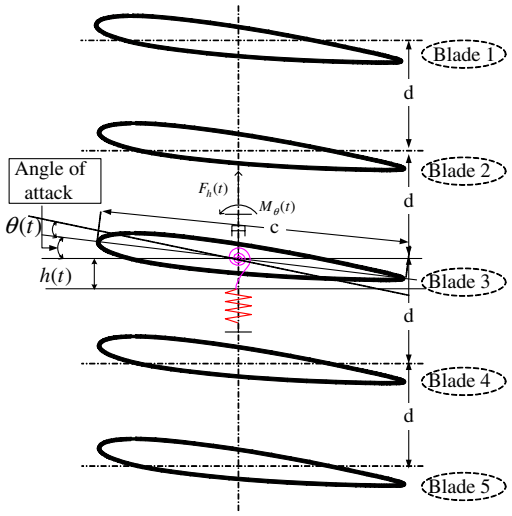

Fig. 4 Oscillating cascade with 2 degrees of freedom.

The following parameters are considered: $m = 1.0$, $c = 1.0$, $a_h = -1$, $x_\theta = 1.8$, $\gamma_\theta = 1.865$, $\xi_h = 0$, $\xi_h = 0$, and $\lambda = 1$. For all of the following simulations, the initial angle of attack is set to 10 and the system damping coefficients ξ_h and ξ_θ are set to zero in order to excite high-amplitude oscillations. The rotational moment F_θ and its coefficient C_M are defined as follows:

$$F_\theta = \int_\Gamma F(\mathbf{x}, t) \times r \, \mathrm{d}\mathbf{x}_s \tag{21}$$

$$C_M = \frac{2F_\theta}{\rho_\infty l^2 U_\infty^2} \tag{22}$$

$$C_{\text{damping}} = -\frac{1}{T\pi h^2} \int_0^T C_L \, \mathrm{d}h + C_M \, \mathrm{d}\theta \tag{23}$$

The damping coefficient is defined by Sadeghi and Liu [11]. Solving Eqs. (18) and (19) with the Newmark-β method, the airfoil instantaneous displacement, velocity, and acceleration vectors can be predicted, and then the airfoil surface boundary condition is updated. The chord length of the blade is 1 and the computational domain is a 4×3 rectangle, which is divided into a 200×150 mesh. The initial angle of attack is set at 10 deg and the cascade spacing between two adjacent blades is set to 0.5. The Reynolds number is set to 100 in this case, with the reference length and velocity chosen to be the chord length and inflow velocity. The blade profile is NACA0012. The discrete points used to describe each airfoil are 181. At the inlet boundary, uniform flow velocities $u = 1$ and $v = 0$ are applied. At the upper and lower boundaries, nonshear conditions are applied, $\frac{\partial u}{\partial y} = 0$ and $v = 0$ and the boundary condition for the airfoil is the nonslip condition. At the outlet boundary, a "buffer domain" is appended to ensure a nonreflecting boundary condition [30].

In this oscillating cascade simulation, the steady solution of the flow past the stationary cascade is set as the initial flowfield and the airfoil is released and starts to move at $t = 0$. The computational domain size effect and the grid dependency study have been done in the flow past a stationary cascade case. As shown in Table 1, the computational size is suitable.

For an actual compressor or turbine oscillating cascade, the IBPA is unknown and depends on the blades, disk, and fluid interaction. Though the computational fluid dynamics and finite element method developed rapidly in the past decades, it is still a difficult task to simulate flow through a full annulus of the compressor or turbine. By simulating the blades, disk, and fluid interaction together, the task becomes almost impossible. For this reason the finite blade passages were chosen to simulate the annulus blades to reduce the time

Table 1 Drag coefficients, lift coefficients, and rotational moment coefficients with different computational domains and mesh numbers

Computational domain and mesh numbers	Drag coefficient	Lift coefficient	Rotational moment coefficient
4×3, 200×150	1.384	0.434	0.105
4×3, 300×225	1.339	0.450	0.102
4×3, 400×300	1.313	0.462	0.0995
6×3, 300×150	1.382	0.423	0.104
8×3, 400×150	1.381	0.422	0.103

consumption; on the other hand, the IBPA and periodic boundary condition are introduced to the model. The aim of introducing the IBPA assumption instead of free aeroelastic vibration to the cascade simulation is to include the effect of the disk vibration and its mode propagation, and the value of IBPA is restricted by the number of blade passages. If the cascade oscillates in an uncoupled way, namely, the motion is given or in harmonic mode, it is easy to satisfy the IBPA condition and periodic boundary condition. For the coupled way, the motion of cascade is obtained by solving the structure equation in each time step; this means it is hard to directly satisfy the IBPA condition. So in this paper, only the structure equation for the prescribed blade is solved. And then the motions of the other neighboring blades depend on the IBPA condition.

Here, the details of how to determine the blade vibration with equal amplitudes and a constant IBPA are given. For the IBPA $= 0$ case, all the other blades are oscillating with the same amplitude as the third blade at the same time. In each time step, we obtain the movement data of the third blade, such as velocity, displacement, by solving the governing equations. And the other blades use the data of the third blade to move. The condition is satisfied directly. For the IBPA $\neq 0$ case, as shown in Fig. 5, the displacements are determined by the following four steps:

1) Setting IBPA $= 0$ as the initial condition, namely, the blades oscillate in the same mode. The temporal series of the movement factors including h, $\dot{h}$, θ, and $\dot{\theta}$ are saved to a stack.

2) After a certain time interval, the oscillating frequency is obtained by applying a real-time fast Fourier transform (FFT) to the temporal series of transverse displacements. The time interval is defined as the oscillating period of corresponding U^*, IBPA $= 0$ case. If the FFT results contain multiple frequencies, we pick the one with the maximum amplitude to calculate the time offset.

3) Using the IBPA and oscillating frequency, the time offsets of the other blades in a temporal series of oscillating amplitude are obtained simply ($\Delta t = \text{IBPA}/2\pi f$).

4) By using the time offsets to get the corresponding temporal series of movement factors from the stack, which has been saved in the first step, the blades move with the actual IBPA.

With this method, the unsteady oscillation with arbitrary IBPA can be calculated. Here, we would like to clarify more details of our method. The key problem with different IBPA is how to obtain the period T or frequency f of the system. Before the computation is carried out, the value of T is unknown. In addition, all the movements of the cascade with different IBPA are in the same way before the FFT is performed. After the period is prescribed at the start point, for a different IBPA case, the time offset is different. So the movement

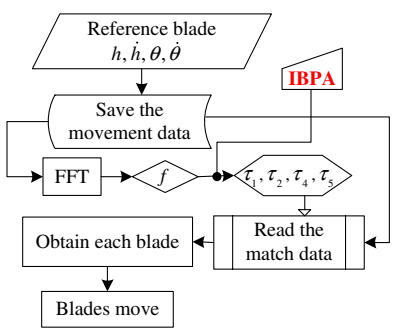

Fig. 5 For the IBPA $\neq 0$ case: the movements computational process.

factors taken from the stack are totally different. The other blades with different movement factors would provide a different "boundary condition." The third blade is totally no restrictions; its frequency and amplitude only depend on the natural frequency and the fluid that surrounds it. The whole system responses are changed by applying different IBPA, so this would not lead to obtain the same oscillation frequency. The stack is updated and a FFT is performed in each time step. In each time step, the new result is pushed into the stack, and the oldest result in time history is deleted. That means the stack is always being updated. On the other hand, how to define the size of the stack is still a problem. Obviously, the best size of the stack is one period. If so, the IBPA condition is obtained more accurately. In fact, the period T is unknown, while performing FFT needs the nth power of 2 (2^n) points in time history. So we define the stack size as 2^{13} (8192). For $U^* = 0.7$, IBPA $= 0$ case, the frequency is 2.44, namely, the given period is 0.40925. The time step size is 0.0005, that means near 818 steps in time evolution of each period. We use 8192 points to store the latest result in the stack, which means the result of the FFT is time averaged by 10 periods. To capture the information more sensitively, the stack size needs to be as small as possible. On the contrary, performing FFT needs a bigger size of the stack to improve the accuracy in the time evolution, namely, to lose the sensitivity.

We still have no good idea about strictly validating the stack size. We have tested, using 2^{12}–2^{15} points (5–40 periods) as the stack size in the present cases does not influence the results. We should emphasis that the present results of the frequency and damping ratio with different U^* and IBPA are not obtained in real time. After the fluid–structure interaction computation, FFT is performed for total time series data. And then, we obtain the time-averaged frequency and time-averaged period (T). This time-averaged period is applied to calculate the damping coefficient and plot the frequency in the figures as a final result.

At the same time we should note that the above procedure may only provide approximate results compared to the real physical phenomena. On the other hand, the models available in the current literatures are also based on the assumptions that the IBPA can be accurately known, whereas the fact is, it is quite difficult to obtain the exact IBPA distribution in the current computational techniques. Therefore, the ultimate solution may be to combine the blades and disk vibration with the relevant flow to simulate their interaction in the domain of full annulus of blade rows.

The reduced velocity is defined as $U^* = U_\infty/f_n D = 2\pi U_\infty/\omega D$, which determines the response of the system. The first set of simulations are carried out with different U^* and the IBPA is fixed at zero; all the other blades are assumed to move with the same motion as the third blade. In the second set of computations, the reduced velocity is fixed at $U^* = 0.7$ and the effect of IBPA ($0 \leq \text{IBPA} \leq 180$) is investigated.

1. *Oscillating Cascade (*IBPA $= 0$*, Variation with* U^**)*

To investigate the effect of reduced velocity U^* on the oscillating cascade, computations are carried out for various values of U^* while the IBPA is fixed at zero. Because the motion of five blades is the same, the following discussion focuses on the third blade.

Figure 6 shows a variation of the reduced frequency of transverse oscillations of the third blade with the reduced velocity U^*. In the same figure, two auxiliary lines are plotted, which shows the variation of the reduced frequency with U^*. We notice from the figure that the reduced frequency of transverse oscillation is close to

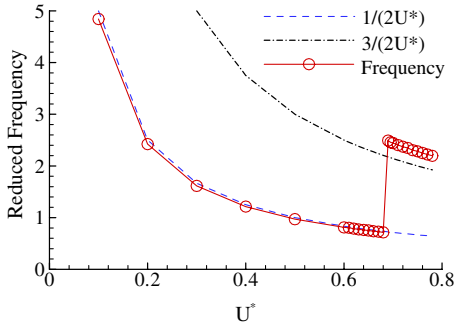

Fig. 6 Variation of the reduced frequency of transverse oscillations of the third blade with reduced velocity, U^*.

$1/(2U^*)$ in the lower range of $U^* < 0.7$. When U^* has an increase close to 0.7, we observe the frequency "jump" phenomena. In a higher range of $U^* > 0.7$, the frequency value is close to $3/(2U^*)$. As Fig. 6 displayed, the third blade oscillating frequency is locked in two frequencies: the first one's value is half of the reduced natural frequency, that is $F_n/2 = 1/(2U^*)$, and the second one's value is triple of the first one, that is, $3/(2U^*)$, for the whole range of U^*. One possible explanation of the decrease of the lock-in frequency is the coupling of transverse movement and rotational movement reduces the system stiffness. When $U^* > 0.7$, the oscillating amplitudes in 2 degrees of freedom are gradually amplified and the oscillating frequency is excited and jumps to the multiple, that is, $3/(2U^*)$. It is well known that the flow past a stationary blade with small angle of attack is a streamline body problem without vortex shedding. The spring-supported blade is forced to move to a certain position to keep the balance of the aerodynamic force and elastic force. As the reduced velocity increases, the vortex formation frequency is close enough to the blade's natural frequency, and this makes the unsteady aerodynamic forces on blade respond to the vortex shedding. In this simulation, it is interesting to note that the nondimensional frequency of lift coefficients, drag coefficients, and rotational moment coefficients is tuned to the same value.

Figure 7 shows the variation of damping coefficients of the third blade with reduced velocity, U^*. In the lower range of U^*, the damping coefficients are positive, and that means the whole system is stable. The amplitudes decrease with the increasing of U^*. When U^* increases close to 0.7, the damping coefficients become negative, and the system is unstable. It is interesting that the damping coefficients jump phenomena is similar to Fig. 6. The system becomes unstable when $U^* > 0.7$, in the same U^* range, the oscillating frequency jumps from $1/(2U^*)$ to $3/(2U^*)$.

Figure 8 show the time evolution of transverse displacements and rotational angles of the airfoil at different U^* values of 0.20, 0.69, 0.7, and 1.0. In the lower range of U^*, though the amplitudes are rather low, the rotational angle and transverse displacement increase with the increasing of U^*. When U^* increases up to 0.7, the rotational angle and transverse displacement rapidly become large and the system becomes unstable; the cascade will oscillate in high amplitude and the oscillation amplitude is amplified rapidly to infinity.

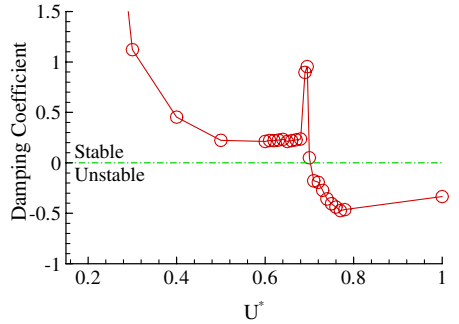

Fig. 7 Variation of the damping coefficient of the third blade with reduced velocity, U^*.

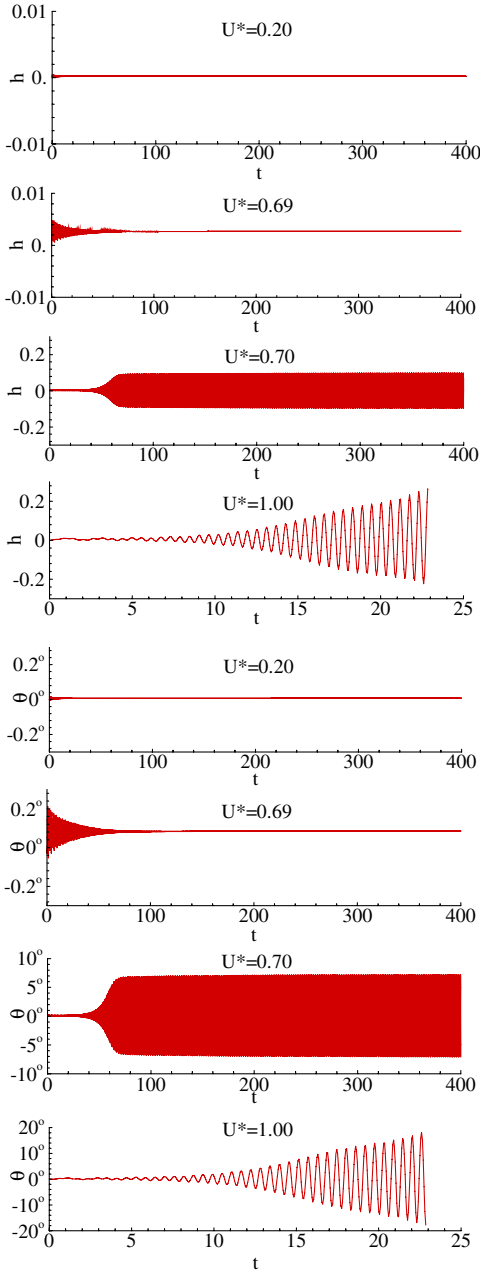

Fig. 8 The time evolution of transverse displacement and rotational angle of the third blade.

It can be seen that in the lower range of U^*, the oscillations of the third blade in 2 degrees of freedom are damped and after a certain time, the blade oscillation would eventually reach a fixed transverse displacement and angle of attack. The damping time is prolonged with the increase of U^*. When U^* approaches 0.7, the oscillation amplitudes in 2 degrees of freedom are not damped or amplified, and the airfoil oscillates in a quasi-steady amplitude and period. As was described previously, in a higher range of $U^* > 0.7$, the oscillation of the cascade is amplified in both transverse movement and angle rotation and the system becomes unstable.

Figure 9 shows the variation of the transverse displacements versus transverse velocities and the rotational angles versus rotational velocities at $U^* = 1.0$, where the system diverges and at $U^* = 0.7$ where the system remains stable, with the small circular spot on the graph indicating the initial movement status. The systems show a different behavior at the two different parameter setups: for $U^* = 0.7$, the blade is attracted to an equilibrium state of oscillation, while for $U^* = 1.0$, the equilibrium state of oscillation seems not steady because all the parameters are amplified fast, which means nonlinear oscillation occurs. Based on the previous analysis, it is

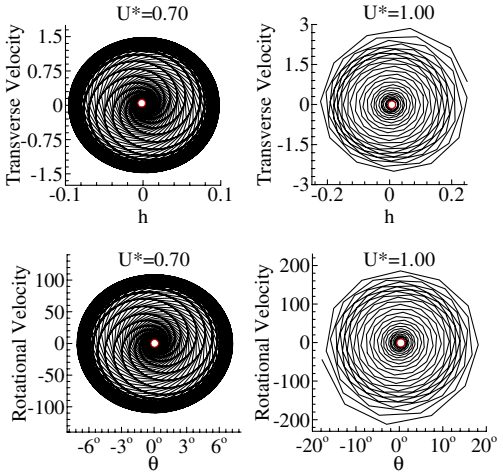

Fig. 9 Comparison: variation of the rotational angle versus rotational velocity, and the transverse displacement versus transverse velocity of the third blade with rotational velocity.

found that U^* is the critical stable boundary at its value close to 0.7 in this case.

From the above various numerical results, the present simulation does capture many interesting and meaningful features of fluid–cascade interaction, such as the nonlinear evolution of blade oscillation, "mode jump," and frequency lock-in phenomena. Besides, the reduced velocity U^* can be considered as one of the most sensitive factors to determine if the cascade oscillation is stable or unstable.

2. *Oscillating Cascade ($U^* = 0.7$, Variation with IBPA)*

The cascade aeroelastic stability has been investigated at a fixed interblade phase angle (IBPA = 0) with different reduced velocity. At the same time, we have noted that reduced velocity $U^* = 0.7$ is quite sensitive for IBPA = 0 in the above given parameters. For comparison, we will further discuss how the cascade aeroelatic stability responds to the variation of IBPA when other parameters stay unchanged.

Figure 10 shows the comparison of instantaneous streamlines of flow past the oscillating cascade in one quasi period with different IBPA. Even for the same reduced velocity ($U^* = 0.7$), the effect of IBPA is totally different. We can clearly observe the totally different vortex forming, stretching, and shedding process from the figure. The streamlines of the IBPA = 180 case become more complex than those for the IBPA = 0 case in time evolution. The cascade spacing between two adjacent blades is constant for IBPA = 0, so the blade is oscillating in synchronal mode. For the IBPA = 180 case, the motion of the adjacent blade is always contrary, and that means the cascade spacing is keeping a variation with the time evolution. In some instantaneous flowfield, the adjacent blades move close to each other, and this results in a decrease of the width of the cascade spacing. The blade passage is similar to a "nozzle." If the adjacent blades move away from each other, the blade passage is similar to a "diffuser." That is why the flow patterns with different IBPA are so different.

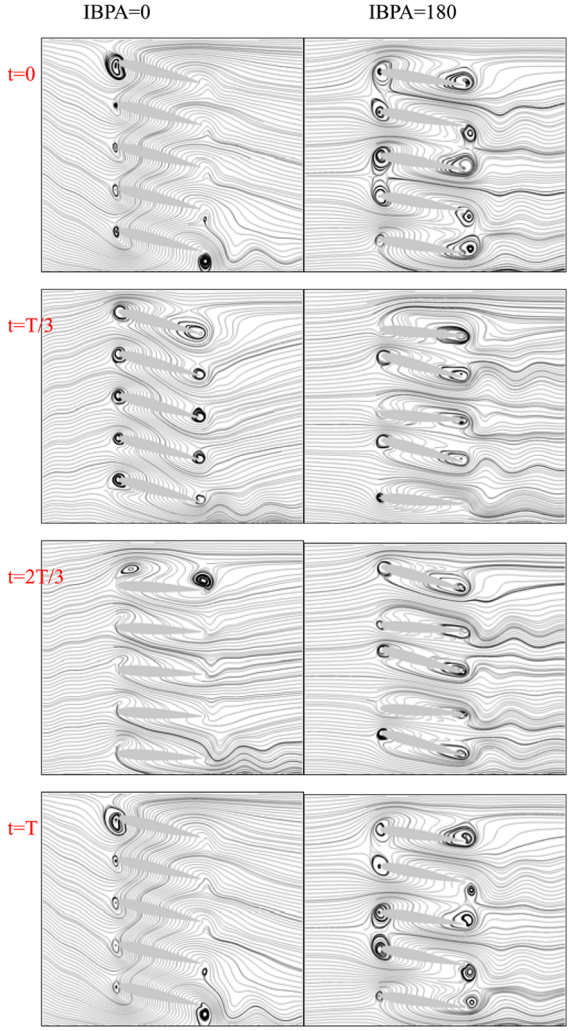

Fig. 10 Comparison: instantaneous streamlines in one quasi period at $U^* = 0.7$.

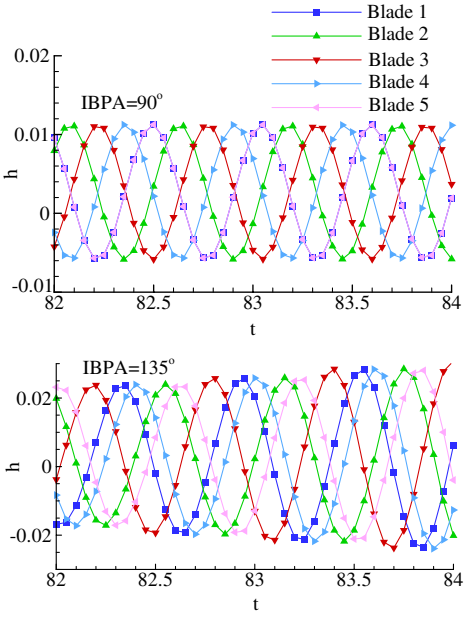

Fig. 11 The time evolution of the transverse displacement of five blades.

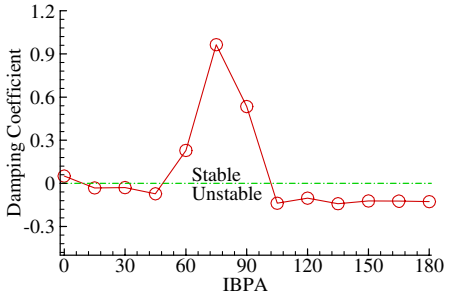

Fig. 12 Variation of the damping coefficient of the third blade with IBPA.

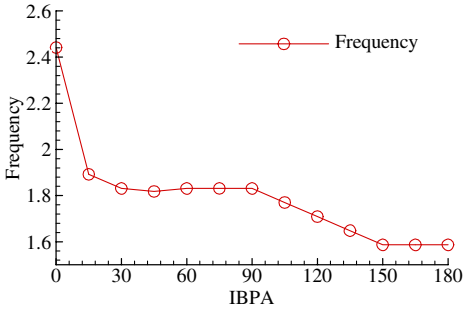

Fig. 13 Variation of the reduced frequency of the third blade with IBPA.

Figure 11 shows the time evolution of transverse displacements of five blades at IBPA = 90 and 135. From these figures we can find that the IBPA conditions are well applied, and the five blades are oscillating in the same amplitude and frequency but correspond to different IBPA. The movement of five blades is similar excluding the IBPA, which is just a phase-lagged phenomenon in time evolution. And so the following discussion focuses on the third blade.

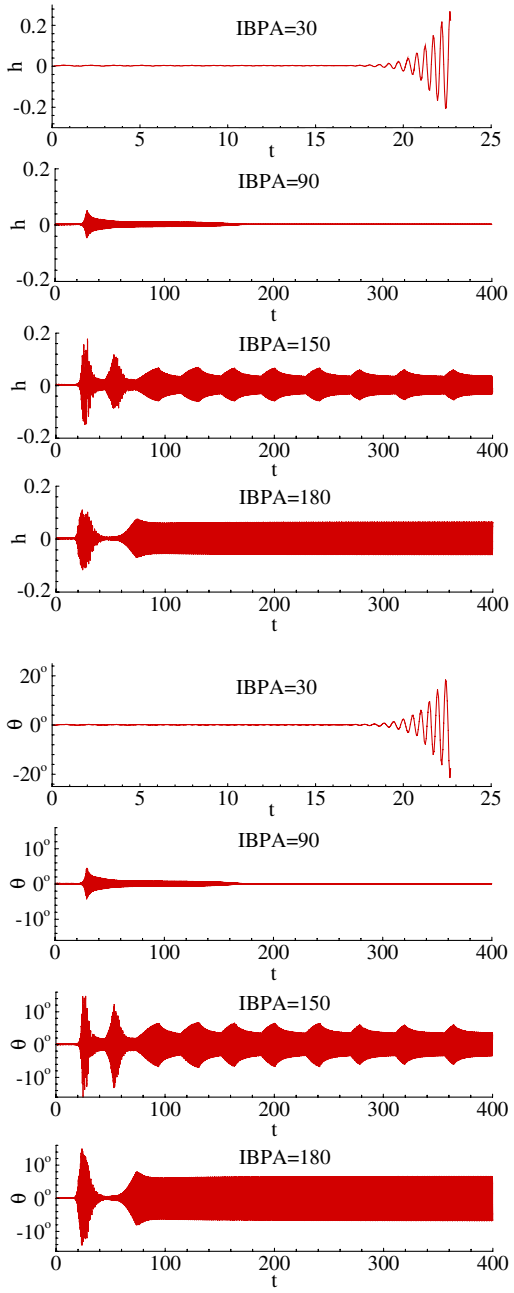

Fig. 14 The time evolution of transverse displacement and rotational angle of the third blade at different IBPA.

From Fig. 12, we find that the IBPA is a sensitive factor, which has a close relation with the system stability. When IBPA = 0, though the damping coefficient is small, the system is stable. And for IBPA = 15, 30, and 45, the value become negative. In fact, the cascade oscillating amplitude is quickly amplified to a rather high magnitude. The phenomena can be observed more clearly in the time history of various parameters. In fact, the damping coefficient is positive and its value is high for IBPA = 60, 75, and 90, meaning the oscillation is damped and the system is stable. When the IBPA is higher than 90, the system is unstable.

It is clear from Fig. 13 that the reduced frequency of the third blade is a function of the IBPA. The reduced frequency value is obtained when the blade achieves the maximum oscillating amplitude with the corresponding IBPA. The most interesting result is that the reduced frequency is monotonously decreasing with the increase of the IBPA. One possible reason is that the coupling of the fluid and the structure reduces the stiffness of the whole system with the increasing of the IBPA.

Figure 14 shows the time evolution of transverse displacements, rotational angles of the third blade at different IBPA (=30, 90, 150, and 180). In the lower range of IBPA (=30), it can be seen that the oscillating amplitudes of the cascade increase rapidly. In this situation, the results are similar to a negative damping example, which may be obtained by the energy method. The aerodynamic forces do not have any damping effect; the oscillation of the cascade is amplified to infinity in both transverse movement and rotational angle, namely, the system becomes unstable. With the increase of the IBPA, the damping effects of the unsteady blade leading seem to appear. When IBPA > 45, though the oscillating is still amplified in a short time, the aerodynamic damping enables the amplitude of vibration to decrease rapidly. We also found that the damping time is prolonged with the increase of the IBPA. Finally, the cascade oscillates in very low amplitude, which is nearly at rest, in a new balance position and a new angle of attack.

Similar to the fixed IBPA case, Fig. 15 shows the variation of the transverse displacements versus transverse velocities and the rotational angles versus rotational velocities of the third blade at IBPA = 30 where the system diverges and at IBPA = 75 where the system remains stable, with the small circular spot on the graph indicating the initial movement status. From the figure, it is found that the IBPA discrepancy changes the response and the stability of the system.

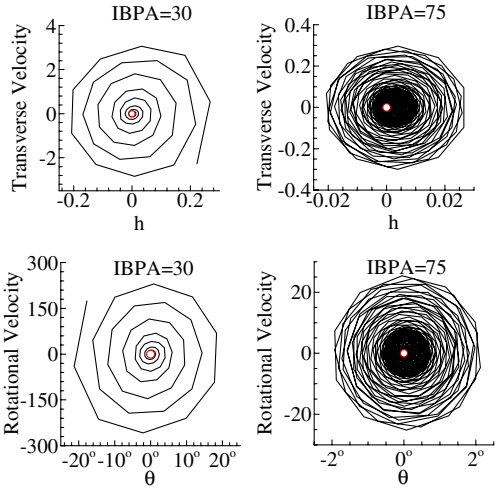

Fig. 15 Comparison: variation of the rotational angle versus rotational velocity, and the transverse displacement versus transverse velocity of the third blade..

IV. Conclusions

This paper combines the immersed-boundary method with the operator splitting technique to investigate two-dimensional fluid–structure interaction problems. The numerical simulation method presented in this paper is first validated by two cases with moving boundary, that is, the oscillating circular cylinder in rest water and the flapping airfoil. With these checks, the present work is extended to investigate the cascade oscillating problem with an emphasis on the physical understanding of the fluid–structure interaction. Especially, this paper presents an analysis to the behavior of the fluid–cascade interaction system at a different parameter setup and discusses its critical stable boundary. We found that the reduced velocity U^* is a very sensitive factor, which affects the critical stable boundary in the present examples. Besides, the IBPA can also change the response and the stability of the system. Also, most of the present results are shown as functions of a temporal series, namely, it is convenient to observe when and how the system becomes unstable, and it may also be useful to reveal more cascade oscillating/flutter mechanisms and deepen our physical understanding.

In this study, we apply the same process without generating any body-fitting grid to several test cases. That means the present method has an obvious advantage of time savings and does not require considering the mesh quality problem. However, further research work is still required to find the reduced velocity and the IBPA corresponding to a critical stable boundary for a real cascade aeroelastic analysis. In particular, the present work only deals with the physical phenomena related to the low Reynolds number and incompressible flow, and considerable work is still required for more complicated fluid–cascade interaction problems.

Acknowledgments

The sponsorships of the National Natural Science Foundation of China (NSFC) (Nos. 10472009, 50736007, 50136010) and 111 project are acknowledged.

References

[1] Huang, X. Y., "Active Control of Aerofoil Flutter," *AIAA Journal*, Vol. 25, No. 8, 1987, pp. 1126–1132. doi:10.2514/3.9753

[2] Sun, X., and Kaji, S., "Effects of Wall Admittance Changes on Aeroelastic Stability of Turbomachines," *AIAA Journal*, Vol. 38, No. 9, 2000, pp. 1525–1533. doi:10.2514/2.1174

[3] Sun, X., Jing, X., and Zhao, H., "Effects of Wall Admittance Changes on Aeroelastic Stability of Turbomachines," *Journal of Propulsion and Power*, Vol. 17, No. 2, 2001, pp. 248–255. doi:10.2514/2.5770

[4] Lu, P. J., Pan, D., and You, H. D., "Acoustic Flutter Control of 3D Transonic Rotor Flow," *Journal of Propulsion and Power*, Vol. 18, No. 5, 2002, pp. 1003–1011. doi:10.2514/2.6048

[5] Whitehead, D. S., "Classical Two-Dimensional Methods," *Manual on Aeroelasticity in Axial Flow Turbomachines*, AGARD, Vol. 1, No. 298, 1987, Chap. 3.

[6] Dowell, E. H., and Hall, K. C., "Modeling of Fluid-Structure Interaction," *Annual Review of Fluid Mechanics*, Vol. 33, 2001, pp. 445–490. doi:10.1146/annurev.fluid.33.1.445

[7] Florea, R., and Hall, K. C., "Sensitivity Analysis of Unsteady Inviscid Flow Through Turbomachinery Cascades," *AIAA Journal*, Vol. 39, No. 6, 2001, pp. 1047–1056. doi:10.2514/2.1445

[8] Li, H. D., and He, L., "Blade Aerodynamic Damping Variation with Rotor-Stator Gap: A Computational Study Using Single-Passage Approach," *Transactions of the ASME, Journal of Turbomachinery*, Vol. 127, No. 3, 2005, pp. 573–579. doi:10.1115/1.1928932

[9] Yang, H., and He, L., "Experimental Study on Linear Compressor Cascade with Three-Dimensional Blade Oscillation," *Journal of Propulsion and Power*, Vol. 20, No. 1, 2004, pp. 180–188. doi:10.2514/1.1280

[10] Moffatt, S., and He, L., "On Decoupled and Fully-Coupled Methods for Blade Forced Response Prediction," *Journal of Fluids and Structures*, Vol. 20, No. 2, 2005, pp. 217–234. doi:10.1016/j.jfluidstructs.2004.10.012

[11] Sadeghi, M., and Liu, F., "Computation of Mistuning Effects on Cascade Flutter," *AIAA Journal*, Vol. 39, No. 1, 2001, pp. 22–28. doi:10.2514/2.1297

[12] Sadeghi, M., and Liu, F., "Investigation of Non-Linear Flutter by a Coupled Aerodynamics and Structural Dynamics Method," AIAA Paper 2001-0573, Jan. 2001.

[13] Carstens, V., Kemme, R., and Schmitt, R., "Coupled Simulation of Flow-Structure Interaction in Turbomachinery," *Aerospace Science and Technology*, Vol. 7, 2003, pp. 298–306. doi:10.1016/S1270-9638(03)00016-6

[14] Kazawa, J., and Watanabe, T., "Numerical Analysis Toward Active Control of Cascade Flutter with Smart Structure," AIAA Paper 2002-4079, July 2002.

[15] Thermann, H., and Niehuis, R., "Unsteady Navier-Stokes Simulation of a Transonic Flutter Cascade Near-Stall Conditions Applying Algebraic Transition Models," *Transactions of the ASME, Journal of Turbomachinery*, Vol. 128, 2006, pp. 474–483. doi:10.1115/1.2183313

[16] Cinnella, P., De Palma, P., Pascazio, G., and Napolitano, M., "A Numerical Method for Turbomachinery Aeroelasticity," *Transactions of the ASME, Journal of Turbomachinery*, Vol. 126, 2004, pp. 310–316. doi:10.1115/1.1738122

[17] McBean, I., Hourigan, K., Thompson, M., and Liu, F., "Prediction of Flutter of Turbine Blades in a Transonic Annular Cascade," *Journal of Fluids Engineering*, Vol. 127, 2005, pp. 1053–1058. doi:10.1115/1.2060731

[18] Rzadkowskia, R., and Gnesinb, V., "3-D Inviscid Self-Excited Vibrations of A Blade Row in the Last Stage Turbine," *Journal of Fluids and Structures*, Vol. 23, 2007, pp. 858–873. doi:10.1016/j.jfluidstructs.2006.12.003

[19] Peskin, C. S., "Flow Patterns Around Heart Valves: A Numerical Method," *Journal of Computational Physics*, Vol. 10, No. 2, 1972, pp. 252–271. doi:10.1016/0021-9991(72)90065-4

[20] Peskin, C. S., "Numerical Analysis of Blood Flow in the Heart," *Journal of Computational Physics*, Vol. 25, No. 3, 1977, pp. 220–252. doi:10.1016/0021-9991(77)90100-0

[21] Mohd-Yusof, J., "Development of Immersed Boundary Methods for Complex Geometries," CTR Annual Research Briefs, Center for Turbulence Research, NASA Ames/Stanford Univ., 1998, pp. 325–336.

[22] Fadlun, E. A., Verzicco, R., Orlandi, P., and Mohd-Yusof, J., "Combined Immersed Boundary Finite-Difference Methods for Three-Dimensional Complex Flow Simulations," *Journal of Computational Physics*, Vol. 161, No. 1, 2000, pp. 35–60. doi:10.1006/jcph.2000.6484

[23] Zhu, L. D., and Peskin, C. S., "Simulation of A Flapping Flexible Filament in A Flowing Soap Film by the Immersed Boundary Method," *Journal of Computational Physics*, Vol. 179, No. 2, 2002, pp. 452–468. doi:10.1006/jcph.2002.7066

[24] Miller, L. A., and Peskin, C. S., "When Vortices Stick: An Aerodynamic Transition in Tiny Insect Flight," *Journal of Experimental Biology*, Vol. 207, No. 17, 2004, pp. 3073–3088. doi:10.1242/jeb.01138

[25] Kalitzin, G., and Iaccarino, G., "Toward Immersed Boundary Simulation of High Reynolds Number Flows," Annual Research Briefs, Center for Turbulence Research, Mechanical Engineering Department, Stanford University, 2003.

[26] Mittal, R., Seshadri, V., and Udaykumar, H. S., "Flutter, Tumble and Vortex Induced Autorotation," *Theoretical and Computational Fluid Dynamics*, Vol. 17, 2004, pp. 165–170. doi:10.1007/s00162-003-0101-5

[27] Sun, M., and Tang, J., "Unsteady Aerodynamic Force Generation by a Model Fruit Fly Wing in Flapping Motion," *Journal of Experimental Biology*, Vol. 205, No. 1, 2002, pp. 55–70.

[28] Wang, Z. J., Birch, J. M., and Dickinson, M. H., "Unsteady Forces and Flows in Low Reynolds Number Hovering Flight: Two Dimensional Computations vs Robotic Wing Experiments," *Journal of Experimental Biology*, Vol. 207, 2004, pp. 449–460. doi:10.1242/jeb.00739

[29] Goldstein, D., Handler, R., and Sirovich, L., "Modeling a No-slip Flow Boundary with an External Force Field," *Journal of Computational Physics*, Vol. 105, No. 2, 1993, pp. 354–366. doi:10.1006/jcph.1993.1081

[30] Saiki, E. M., and Biringen, S., "Numerical Simulation of a Cylinder in Uniform Flow: Application of a Virtual Boundary Method," *Journal of Computational Physics*, Vol. 123, No. 2, 1996, pp. 450–465. doi:10.1006/jcph.1996.0036

[31] Peskin, C. S., "The Immersed Boundary Method," *Acta Numerica*, Vol. 11, 2002, pp. 479–517. doi:10.1017/S0962492902000077

[32] Xu, S., and Wang, Z. J., "An Immersed Interface Method for Simulating the Interaction of a Fluid with Moving Boundaries," *Journal of Computational Physics*, Vol. 216, No. 2, 2006, pp. 454–493. doi:10.1016/j.jcp.2005.12.016

[33] Dutsch, H., Durst, F., Becker, S., and Lienhart, H., "Low-Reynolds-Number Flow Around an Oscillating Circular Cylinder at Low Keulegan-Carpenter Numbers," *Journal of Fluid Mechanics*, Vol. 360, 1998, pp. 249–279. doi:10.1017/S002211209800860X

[34] Piperno, S., "Explicit/Implicit Fluid/Structure Staggered Procedures with A Structural Predictor and Fluid Subcycling for 2D Invicid Aeroelastic Simulations," *International Journal for Numerical Methods in Fluids*, Vol. 25, 1997, pp. 1207–1226. doi:10.1002/(SICI)1097-0363(19971130)25:10<1207::AID-FLD616>3.0.CO;2-R

F. Liu
Associate Editor